

Zeptosecond precision pulse shaping

Jens Köhler, Matthias Wollenhaupt,* Tim Bayer,
Cristian Sarpe, and Thomas Baumert

Universität Kassel, Institut für Physik und Center for Interdisciplinary Nanostructure Science
and Technology (CINSA-T), Heinrich-Plett-Straße 40, D-34132 Kassel, Germany

*wollenha@physik.uni-kassel.de

<http://www.physik.uni-kassel.de/exp3.html>

Abstract: We investigate the temporal precision in the generation of ultrashort laser pulse pairs by pulse shaping techniques. To this end, we combine a femtosecond polarization pulse shaper with a polarizer and employ two linear spectral phase masks to mimic an ultrastable common-path interferometer. In an all-optical experiment we study the interference signal resulting from two temporally delayed pulses. Our results show a 2σ -precision of $300 \text{ zs} = 300 \times 10^{-21} \text{ s}$ in pulse-to-pulse delay. The standard deviation of the mean is 11 zs. The obtained precision corresponds to a variation of the arm's length in conventional delay stage based interferometers of 0.45 \AA . We apply these precisely generated pulse pairs to a strong-field quantum control experiment. Coherent control of ultrafast electron dynamics via photon locking by temporal phase discontinuities on a few attosecond timescale is demonstrated.

© 2011 Optical Society of America

OCIS codes: (270.1670) Coherent optical effects; (320.0320) Ultrafast optics; (320.5540) Pulse shaping; (320.7080) Ultrafast devices; (320.7100) Ultrafast measurements; (020.2649) Strong field laser physics; (020.4180) Multiphoton processes.

References and links

1. A. W. Albrecht, J. D. Hybl, S. M. Gallagher Faeder, and D. M. Jonas, "Experimental distinction between phase shifts and time delays: Implications for femtosecond spectroscopy and coherent control of chemical reactions," *J. Chem. Phys.* **111**, 10934–10956 (1999).
2. D. J. Tannor, R. Kosloff, and S. A. Rice, "Coherent pulse sequence induced control of selectivity of reactions: Exact quantum mechanical calculations," *J. Chem. Phys.* **85**, 5805–5820 (1986).
3. M. A. Bouchene, V. Blanchet, C. Nicole, N. Melikechi, B. Girard, H. Ruppe, S. Rutz, E. Schreiber, and L. Wöste, "Temporal coherent control induced by wave packet interferences in one and two photon atomic transitions," *Eur. Phys. J. D* **2**, 131–141 (1998).
4. A. Präkelt, M. Wollenhaupt, C. Sarpe-Tudoran, and T. Baumert, "Phase control of a two-photon transition with shaped femtosecond laser-pulse sequences," *Phys. Rev. A* **70**, 063407 (2004).
5. M. Wollenhaupt, A. Assion, D. Liese, Ch. Sarpe-Tudoran, T. Baumert, S. Zamith, M. A. Bouchene, B. Girard, A. Flettner, U. Weichmann, and G. Gerber, "Interferences of ultrashort free electron wave packets," *Phys. Rev. Lett.* **89**, 173001 (2002).
6. M. Wollenhaupt, A. Assion, O. Bazhan, Ch. Horn, D. Liese, Ch. Sarpe-Tudoran, M. Winter, and T. Baumert, "Control of interferences in an Autler-Townes doublet: Symmetry of control parameters," *Phys. Rev. A* **68**, 015401(R) (2003).
7. M. Wollenhaupt, V. Engel, and T. Baumert, "Femtosecond laser photoelectron spectroscopy on atoms and small molecules: prototype studies in quantum control," *Annu. Rev. Phys. Chem.* **56**, 25–56 (2005).
8. Th. Ergler, A. Rudenko, B. Feuerstein, K. Zrost, C. D. Schröter, R. Moshhammer, and J. Ullrich, "Time-resolved imaging and manipulation of H_2 fragmentation in intense laser fields," *Phys. Rev. Lett.* **95**, 093001 (2005).
9. K. Ohmori, "Development of ultrahigh-precision coherent control and its applications," *Proc. Jpn. Acad., Ser. B* **84**, 167–175 (2008).

10. K. Ohmori, "Wave-packet and coherent control dynamics," *Annu. Rev. Phys. Chem.* **60**, 487–511 (2009).
11. H. Katsuki, K. Hosaka, H. Chiba, and K. Ohmori, "Read and write amplitude and phase information by using high-precision molecular wave-packet interferometry," *Phys. Rev. A* **76**, 013403 (2007).
12. M. Chini, H. Mashiko, H. Wang, S. Chen, C. Yun, S. Scott, S. Gilbertson, and Z. Chang, "Delay control in attosecond pump-probe experiments," *Opt. Express* **17**, 21459–21464 (2009).
13. A. M. Weiner, "Femtosecond pulse shaping using spatial light modulators," *Rev. Sci. Instrum.* **71**, 1929–1960 (2000).
14. A. Monmayrant, S. Weber, and B. Chatel, "A newcomer's guide to ultrashort pulse shaping and characterization," *J. Phys. B* **43**, 103001 (2010).
15. T. Brixner and G. Gerber, "Femtosecond polarization pulse shaping," *Opt. Lett.* **26**, 557–559 (2001).
16. T. Suzuki, S. Minemoto, T. Kanai, and H. Sakai, "Optimal control of multiphoton ionization processes in aligned I₂ molecules with time-dependent polarization pulses," *Phys. Rev. Lett.* **92**, 133005 (2004).
17. T. Brixner, G. Krampert, T. Pfeifer, R. Selle, G. Gerber, M. Wollenhaupt, O. Graefe, C. Horn, D. Liese, and T. Baumert, "Quantum control by ultrafast polarization shaping," *Phys. Rev. Lett.* **92**, 208301 (2004).
18. L. Polachek, D. Oron, and Y. Silberberg, "Full control of the spectral polarization of ultrashort laser pulses," *Opt. Lett.* **31**, 631–633 (2006).
19. M. Ninck, A. Galler, T. Feurer, and T. Brixner, "Programmable common-path vector field synthesizer for femtosecond pulses," *Opt. Lett.* **32**, 3379–3381 (2007).
20. M. Wollenhaupt, M. Krug, J. Köhler, T. Bayer, C. Sarpe-Tudoran, and T. Baumert, "Photoelectron angular distributions from strong-field coherent electronic excitation," *Appl. Phys. B* **95**, 245–259 (2009).
21. D. Kupka, P. Schlup, and R. A. Bartels, "Simplified ultrafast pulse shaper for tailored polarization states using a birefringent prism," *Rev. Sci. Instrum.* **80**, 053110 (2009).
22. F. Weise and A. Lindinger, "Full control over the electric field using four liquid crystal arrays," *Opt. Lett.* **34**, 1258–1260 (2009).
23. C. T. Middleton, D. B. Strasfeld, and M. T. Zanni, "Polarization shaping in the mid-IR and polarization-based balanced heterodyne detection with application to 2D IR spectroscopy," *Opt. Express* **17**, 14526–14533 (2009).
24. M. T. Seidel, S. Yan, and H.-S. Tan, "Mid-infrared polarization pulse shaping by parametric transfer," *Opt. Lett.* **35**, 478–480 (2010).
25. A. Präkelt, M. Wollenhaupt, A. Assion, Ch. Horn, C. Sarpe-Tudoran, M. Winter, and T. Baumert, "Compact, robust, and flexible setup for femtosecond pulse shaping," *Rev. Sci. Instrum.* **74**, 4950–4953 (2003).
26. M. M. Wefers and K. A. Nelson, "Generation of high-fidelity programmable ultrafast optical waveforms," *Opt. Lett.* **20**, 1047–1049 (1995).
27. M. M. Wefers and K. A. Nelson, "Space-time profiles of shaped ultrafast optical waveforms," *IEEE J. Quantum Electron.* **32**, 161–172 (1996).
28. B. J. Sussman, R. Lausten, and A. Stolow, "Focusing of light following a 4-*f* pulse shaper: considerations for quantum control," *Phys. Rev. A* **77**, 043416 (2008).
29. F. Frei, A. Galler, and T. Feurer, "Space-time coupling in femtosecond pulse shaping and its effects on coherent control," *J. Chem. Phys.* **130**, 034302 (2009).
30. B. von Vacano, T. Backup, and M. Motzkus, "*In situ* broadband pulse compression for multiphoton microscopy using a shaper-assisted collinear SPIDER," *Opt. Lett.* **31**, 1154–1156 (2006).
31. B. von Vacano, T. Backup, and M. Motzkus, "Shaper-assisted collinear SPIDER: fast and simple broadband pulse compression in nonlinear microscopy," *J. Opt. Soc. Am. B* **24**, 1091–1100 (2007).
32. A. Galler and T. Feurer, "Pulse shaper assisted short laser pulse characterization," *Appl. Phys. B* **90**, 427–430 (2008).
33. M. Wollenhaupt, A. Assion, and T. Baumert, "Femtosecond laser pulses: linear properties, manipulation, generation and measurement," in *Springer Handbook of Lasers and Optics*, F. Träger, ed. (Springer, 2007), pp. 937–983.
34. R. N. Bracewell, *The Fourier Transform and Its Applications* (McGraw-Hill, 2000).
35. M. Wollenhaupt, D. Liese, A. Präkelt, C. Sarpe-Tudoran, and T. Baumert, "Quantum control by ultrafast dressed states tailoring," *Chem. Phys. Lett.* **419**, 184–190 (2006).
36. M. Wollenhaupt, A. Präkelt, C. Sarpe-Tudoran, D. Liese, T. Bayer, and T. Baumert, "Femtosecond strong-field quantum control with sinusoidally phase-modulated pulses," *Phys. Rev. A* **73**, 063409 (2006).
37. T. Bayer, M. Wollenhaupt, and T. Baumert, "Strong-field control landscapes of coherent electronic excitation," *J. Phys. B* **41**, 074007 (2008).
38. T. Bayer, M. Wollenhaupt, C. Sarpe-Tudoran, and T. Baumert, "Robust photon locking," *Phys. Rev. Lett.* **102**, 023004 (2009).
39. S. Rausch, T. Binhammer, A. Harth, F. X. Kärtner, and U. Morgner, "Few-cycle femtosecond field synthesizer," *Opt. Express* **16**, 17410–17419 (2008).
40. D. Oron, Y. Silberberg, N. Dudovich, and D. M. Villeneuve, "Efficient polarization gating of high-order harmonic generation by polarization-shaped ultrashort pulses," *Phys. Rev. A* **72**, 063816 (2006).
41. C. Ott, P. Raith, and T. Pfeifer, "Sub-cycle strong-field interferometry," *Opt. Express* **18**, 24307–24315 (2010).

1. Introduction

In the past two decades, with the availability of ultrafast lasers and the associated optical techniques, coherent ultrashort light pulses have become an extremely powerful tool for the investigation, manipulation and control of ultrafast processes occurring on timescales down to the attosecond regime. Especially, pairs of ultrashort laser pulses have been a matter of particular interest due to their controllable temporal delay and the relative phase shift between the two pulses [1]. Pump-probe experiments are at the heart of femtosecond spectroscopy and also build the basis for time-resolved studies in the rapidly emerging field of attosecond science. For example, in coherent quantum control, basic control scenarios such as the *Tannor-Kosloff-Rice* scheme [2] are based on precisely timed pulse pairs to exert control on molecular dynamics on the femtosecond timescale. Double pulses have also been used to control *electron* dynamics, e.g. atomic excitation in weak fields [3, 4], interference of ultrashort free electron wave packets [5], and strong field control by Selective Population Of Dressed States (SPODS) [6, 7].

A common requirement for all these experiments is a suitable technique to reliably produce such two-pulse sequences. Generally, interferometric setups, e.g. a Michelson or Mach-Zehnder configuration, are employed for this purpose. In these interferometers a single input pulse is split into two replicas, which travel different pathways. In order to introduce the required temporal separation of the two pulses, the optical path length difference between the two interferometer arms is adjusted. In most cases this is realized by employing mechanical or piezo-based delay stages. Eventually, the two temporally delayed pulses are recombined to propagate collinearly to the experiment. The major challenges in the interferometrical generation of pulse pairs are precision and stability in pulse-to-pulse delay. Generally, interferometers suffer from environmental perturbations, e.g. air flow, mechanical vibrations and thermal drifts, leading to instabilities in the optical path length difference between the two interferometer arms.

Great efforts have been undertaken to address all these issues resulting in interferometer arrangements with enhanced precision and stability. A Mach-Zehnder setup with a resolution better than 0.3 fs being stable during the data acquisition time of more than 50 hours has been reported for time-resolved fragmentation studies in intense laser fields [8]. In [9, 10] (and references therein) high precision coherent control experiments based on pairs of femtosecond laser pulses being phase-locked within the attosecond timescale are presented. In these experiments the pulse pairs are generated by a highly stabilized Michelson interferometer assembled inside a vacuum chamber. The interpulse delay is tuned using a mechanical delay stage in combination with a pressure-controlled gas cell. Control of the stability and resolution down to ± 20 as [11] is realized via a feedback-loop, which compensates drifts in a spectral interferogram produced by the two delayed pulses. Recently, the issue of interferometer instabilities has also been addressed in view of delay control in attosecond pump-probe experiments [12]. In the presented interferometer setup a piezoelectric delay stage has been used to introduce the path length difference between the two arms. This difference has been actively stabilized with the help of a feedback-loop by analyzing and compensating drifts in the interference pattern of a copropagating cw laser. Control of the pulse-to-pulse delay with a precision of 20 as RMS has been demonstrated.

In this paper, we report on an all-optical technique to implement an extremely stable high precision interferometer for ultrashort laser pulse applications, which is based on spectral femtosecond pulse shaping [13, 14]. We make use of a femtosecond polarization pulse shaper [15–24] (and references therein) to mimic a jitter-eliminated common-path interferometer. In our all-optical interferometer, the pulses are not spatially separated and there are no moving mechanical parts. Because of this inherent passive stability, no active stabilization via any kind of feedback-loop is required. In an all-optical experiment we explore the limits of this pulse shaper based interferometer and demonstrate a 2σ -precision of $300 \text{ zs} = 300 \times 10^{-21} \text{ s}$ in pulse-

to-pulse delay. The observed standard deviation of the mean is 11 zs. So far, pulse shaping with sub-attosecond accuracy has not been shown experimentally. Our results demonstrate an improvement on the precision of interferometrically stable generation of pulse pairs by two orders of magnitude.

An application of this technique is presented in a strong-field coherent quantum control experiment, where we make use of these precisely generated pulse pairs to demonstrate coherent control of electron dynamics. Because electrons are much lighter than nuclei, their dynamics is much faster. Therefore, attosecond techniques are commonly considered to be the appropriate tools to efficiently manipulate electron dynamics. However, in this contribution we demonstrate that ultrafast electron dynamics is controlled on the sub-10 as timescale employing a pair of precisely timed femtosecond laser pulses with a temporal separation controllable down to zeptosecond precision.

This paper is organized as follows. In Sect. 2 we start with a description of our pulse shaping setup. First we give an overview of the general layout, then we explain in detail the way to mimic a high-precision common-path interferometer. The all-optical experiment exhibiting a 2σ -precision of 300 zs is presented and discussed in Sect. 3. In Sect. 4 we demonstrate the application of precisely generated double pulses to coherent electronic excitation. An application to attosecond pump-probe experiments is proposed in Sect. 5. We end this article with a brief summary and conclusions in Sect. 6. In the appendix details about the data evaluation of the all-optical experiment are given.

2. Pulse shaper

2.1. General layout

Our home-built polarization pulse shaper is based on a previous design of a compact and robust phase-only modulator [25]. It consists of a folded $4f$ -zero dispersion compressor setup with a double layer Liquid Crystal-Spatial Light Modulator (LC-SLM) located in the Fourier plane. Instead of the transmission grating layout described in [20] we use a slightly modified version for the experiments discussed in this paper. Here, the $4f$ -setup is equipped with 1480 grooves/mm gold-coated reflection gratings (*HORIBA Jobin Yvon*) specifically designed for ultrashort laser pulse compression. The gratings are mounted in Littrow configuration with an angle of incidence of 36.3° . For p-polarized light they possess diffraction efficiencies of more than 85 % for all spectral components in the wavelength range from 700 nm to 900 nm. The efficiency values for s-polarized light lie at about 29 %. Cylindrical mirrors with silver coating and protection layer having a focal length of $f = 223$ mm are used as focusing elements. The 2×640 pixel LC-SLM (*Jenoptik SLM-S640d*) has two independent LC layers with preferential orientation axes at $\mp 45^\circ$ (see Fig. 1). This allows for simultaneous and independent spectral phase modulation of two orthogonally polarized electric field components of the incident light. The existing LC configuration provides the possibility for phase and polarization pulse shaping [20] as well as phase and amplitude modulation by employing an additional polarizer [26]. For polarization pulse shaping the difference between the grating efficiencies for p- and s-polarized light has to be taken into account [15, 20]. If the pulse shaper is used for phase- and amplitude modulation the incoming and outgoing light is generally p-polarized to use the maximum power throughput. In this case the difference between the efficiencies does not play a role.

The phase versus voltage response of both LC layers of the SLM is addressed with a resolution of 12 bit and has been carefully calibrated based on optical transmission measurements similar to the standard procedure described in [13]. When phase functions are inscribed on the LC-SLM small differences in the phase calibration curves between the two layers together with the dispersion properties of the LC are taken into account. This approach ensures implementation of the desired phases at the highest possible accuracy. The spectral transmission window

of the pulse shaper ranges from 719 nm to 873 nm with a central wavelength of 800 nm. It is defined by the spectral components covering the two outer pixels of the LC modulator. The spectral resolution is 0.24 nm/pixel at 800 nm. Spatiotemporal effects as described in [27–29] (and references therein) are minimized in our pulse shaping device due to a proper design. We have realized a compact setup by using cylindrical mirrors with short focal length and highly dispersive gratings to fulfill the design requirements for the minimization of space-time coupling deduced in the above publications. Furthermore, a large input beam diameter ensures narrow spectral component spot sizes in the Fourier plane much smaller than the pixel width. This reduces spanning of several LC-SLM pixels by a narrow spectral band as far as possible. In all our experiments based on the pulse shaper presented in this paper – independent of the employed light source – we use an $1/e^2$ -intensity input beam diameter of more than 3.2 mm. For all wavelengths within the pulse shaper’s spectral transmission window this results in $1/e^2$ -intensity beam diameters in the Fourier plane of less than 78 μm being well below the pixel width of 96.52 μm . In [27,29] a space-time coupling constant primarily determined by the grating parameters is used to quantify spatiotemporal effects. For our pulse shaper setup we obtain an absolute value of 0.2 mm/ps. In addition, by generating double pulses with a delay of about 10 ps and investigating the introduced spatial beam displacement, we verified experimentally that space-time coupling effects are well below the theoretically predicted value.

2.2. Mimicking an interferometer

Making use of both the phase and the amplitude modulation capabilities of our two-layer LC-SLM based pulse shaper, any arbitrary linearly polarized temporal pulse structure can be generated – as long as it is supported by the spectrum of the input pulse. In particular, this scheme makes it possible to create pairs of pulses, each of which is a scaled replica of the initial input pulse [30–32]. This pulse shaper based interferometer is a common-path setup, which guarantees an inherent spatial and – if no phases are applied to the LC-SLM – temporal overlap of the two pulses. Therefore, no alignment issues need to be addressed. This setup is a convenient and ultrastable, i.e. jitter-free, realization of an interferometer for ultrashort laser pulse applications.

Because femtosecond laser pulses are too short to be shaped directly in the time domain, they are modulated in the frequency domain. Optical Fourier transform between these two domains utilizing a $4f$ -setup builds the basis for femtosecond pulse shaping. The incoming real temporal electric field $E_{\text{in}}(t)$ is transformed into its spectral counterpart $\tilde{E}_{\text{in}}(\omega)$, to which a complex spectral transfer function $\tilde{M}(\omega)$ is applied, resulting in a modulated field

$$\tilde{E}_{\text{out}}(\omega) = \tilde{M}(\omega) \cdot \tilde{E}_{\text{in}}(\omega). \quad (1)$$

Performing an inverse Fourier transform this spectral field is transformed back into the time domain to obtain the shaped pulse $E_{\text{out}}(t)$. In order to use a pulse shaper to mimic an interferometer, the temporal electric field $E_{\text{out}}(t) = \frac{1}{2} [E_{\text{in}}(t - \frac{\tau}{2}) + E_{\text{in}}(t + \frac{\tau}{2})]$ is created. Employing the Fourier shift theorem, we find the corresponding spectral electric field $\tilde{E}_{\text{out}}(\omega) = \frac{1}{2} [\exp(-i\omega\frac{\tau}{2}) + \exp(i\omega\frac{\tau}{2})] \cdot \tilde{E}_{\text{in}}(\omega) = \cos(\omega\frac{\tau}{2}) \cdot \tilde{E}_{\text{in}}(\omega)$. A comparison of this expression with Eq. (1) shows, that the incoming spectral electric is modulated by a cos-function. Generalizing this spectral transfer function for the generation of a pair of identical pulses with temporal delay τ by the introduction of a reference frequency ω_{ref} , it reads

$$\tilde{M}(\omega) = \cos\left[(\omega - \omega_{\text{ref}})\frac{\tau}{2}\right] = \left| \cos\left[(\omega - \omega_{\text{ref}})\frac{\tau}{2}\right] \right| \text{sgn}\left\{ \cos\left[(\omega - \omega_{\text{ref}})\frac{\tau}{2}\right] \right\}, \quad (2)$$

Depending on the value of ω_{ref} either only the envelopes of the two pulses or both the envelopes and the relative phase between the two pulses are shifted upon scanning the pulse-to-pulse delay τ . The first mode is achieved by the choice $\omega_{\text{ref}} = \omega_0$, where ω_0 is the central frequency

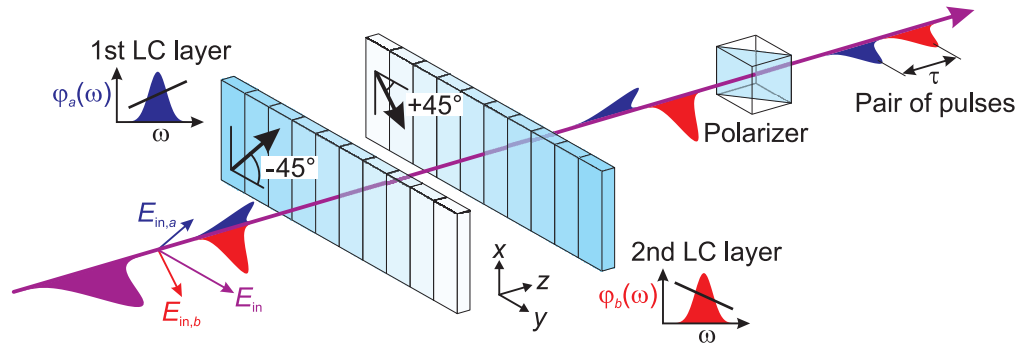


Fig. 1. (Color online) Mimicking an interferometer by the use of a double layer LC-SLM based pulse shaper. The horizontally polarized electric field E_{in} of the input pulse is represented as a superposition of two linearly polarized components $E_{in,a}$ and $E_{in,b}$ with orthogonal polarization planes at $\pm 45^\circ$. Each of these two components is individually modulated by one of the LC layers. The bold arrows on the layers indicate the preferential orientation axes of the LC molecules. By applying appropriate linear spectral phase functions $\varphi_a(\omega)$ and $\varphi_b(\omega)$ the input pulse is split into two identical temporally delayed replicas with crossed linear polarizations. A subsequent polarizer projects the polarization directions of the two pulses onto the same plane. The pulse energy ratio between the two pulses is tuned, e.g. by rotating the polarization plane of the input pulse using a half-wave plate (not shown here).

of the incoming laser pulses. The second mode describes the situation in a conventional interferometer. It is realized by setting $\omega_{ref} = 0$. Generally, the required optical transfer functions are calculated employing Fourier techniques. In the following we present an alternative and intuitive approach to obtain the transfer function needed for pulse shaper based interferometry (cf. Eq. (2)). Our scheme builds on basic principles of spectral phase-only modulation.

Considering the manipulation of ultrashort laser pulses, it is common – as well as sufficient for many applications – to expand the spectral phase function into a Taylor series. This approach allows an independent treatment of the terms of different orders and to discuss their influence on the temporal pulse structure separately. In order to realize a pulse shaper based interferometer only the coefficients up to the first order are relevant. The zeroth order coefficient describes the carrier-envelope phase (absolute phase) of the pulse in the time domain. The first order coefficient, i.e. the linear term, is related to a temporal shift of the envelope [1, 4, 33]. Depending on the choice of the reference frequency ω_{ref} the absolute phase may be changed in addition. Typically, as depicted in Fig. 1, the electric field of the initial pulse entering the pulse shaper is linearly polarized (p-polarized). Its polarization plane is oriented at $\pm 45^\circ$ with respect to the preferential orientation axes of the LC layers. The spectral electric field $\tilde{E}_{in}(\omega)$ of the input pulse is considered to be a superposition of two identical linearly polarized components $\tilde{E}_{in,a}(\omega)$ and $\tilde{E}_{in,b}(\omega)$. These components are polarized orthogonally with respect to each other. One polarization plane is parallel to the orientation axis of the first LC layer, the other polarization plane is parallel to the axis of the second LC layer. As described above our pulse shaper provides the capability to modulate the spectral phases of both components independently. By applying the phases

$$\varphi_a(\omega) = \phi_{0,a} + \tau_a(\omega - \omega_{ref}) \quad (3)$$

$$\varphi_b(\omega) = \phi_{0,b} + \tau_b(\omega - \omega_{ref}) \quad (4)$$

to the electric field components $\tilde{E}_{\text{in},a}(\omega)$ and $\tilde{E}_{\text{in},b}(\omega)$, the carrier-envelope phases and the temporal positions of the two corresponding pulses are completely controlled. Choosing suitable values for the phase function parameters $\phi_{0,a}$, τ_a , $\phi_{0,b}$ and τ_b , the initial input pulse is split into two identical temporally delayed replica with crossed polarizations. A projection onto the same plane is realized by the use of a subsequent polarizer. The combination of two $\mp 45^\circ$ LC layers followed by a polarizer with transmission axis at 0° , i.e. parallel to the y -axis (see Fig. 1), is mathematically expressed by the Jones-matrix [13]

$$\hat{J}(\omega) = \exp\left(-i\frac{\varphi_a(\omega) + \varphi_b(\omega)}{2}\right) \cos\left(\frac{\varphi_a(\omega) - \varphi_b(\omega)}{2}\right) \begin{pmatrix} 0 & 0 \\ 0 & 1 \end{pmatrix}. \quad (5)$$

Inserting the phase functions given in Eqs. (3) and (4) into this matrix (Eq. (5)) using the parameters $\phi_{0,a} = \phi_{0,b} = 0$, $\tau_a = +\frac{\tau}{2}$, $\tau_b = -\frac{\tau}{2}$ and evaluating the influence of the resulting expression on light linearly polarized along the y -axis, we directly obtain the transfer function given in Eq. (2).

The transfer function given in Eq. (2) splits the initial input pulse into two identical replicas with the same energies. In order to generate two scaled replicas of the input pulse with unequal energies, a different transfer function is needed. The one to create the field $E_{\text{out}}(t) = A \cdot E_{\text{in}}(t - \frac{\tau}{2}) + B \cdot E_{\text{in}}(t + \frac{\tau}{2})$ with $A + B \leq 1$ must be calculated. Following our intuitive scheme, we make use of a different approach. Without changing the phase functions applied to the LC-SLM we tune the ratio of the pulse energies simply by changing the energy ratio of the two components $\tilde{E}_{\text{in},a}(\omega)$ and $\tilde{E}_{\text{in},b}(\omega)$ of the input field $\tilde{E}_{\text{in}}(\omega)$. A rotation of the polarization plane of the linearly polarized input pulse employing a half-wave plate leads to an unequal energy distribution of the two components at $\mp 45^\circ$. Rotation angles of the polarization plane between -45° and $+45^\circ$ allow the realization of any desired pulse energy ratio. After rotation of its polarization plane, the incoming light is still linearly polarized for our reflection gratings, but it is not p-polarized any more. It is a superposition of p- and s-polarized components. Therefore, the difference between the grating efficiencies for p- and s-polarized light (cf. Subsection 2.1) has to be taken into account to determine the rotation angle of the half-wave plate needed for a certain energy ratio of the two pulses. The situation $A + B < 1$ corresponds to an additional attenuation reducing the total amount of energy contained in the pair of pulses.

This intuitive approach to mimic an interferometer by the use of a pulse shaper is a general and widely applicable scheme. It is not restricted to the use of linear phase functions on the LC-SLM. In addition to the linear terms determining the pulse-to-pulse delay τ , any arbitrary phase modulation can be applied. Thus, the double layer LC-SLM based pulse shaper cannot only be used to mimic an interferometer, but it may serve as an interferometer with independent spectral phase modulators in both arms giving access to a large class of shaped pulse pairs.

3. All-optical experiment

3.1. Experimental

In order to investigate the limit in temporal precision in the adjustment of the separation of two ultrashort laser pulses, we performed an all-optical experiment. The pulse shaper was used to mimic an interferometer as described in Subsect. 2.2. The optical interference signal S of two temporally overlapping identical pulses was recorded as a function of the pulse-to-pulse delay τ with a photodiode located directly behind the shaper to produce a 1st order interferometric autocorrelation. This signal was measured for different delay intervals with successively decreasing ranges and employing decreasing step sizes. In order to maximize the signal to noise ratio we chose a femtosecond oscillator as light source for this experiment. The used Ti:sapphire oscillator (*Femtolasers Fusion Pro 400*) has a repetition rate of 75 MHz, a pulse energy of about 6.5 nJ and a spectral bandwidth of more than 80 nm Full-Width at Half Maximum (FWHM) centered

at 800 nm. The latter results in a duration of less than 12 fs FWHM for the bandwidth-limited pulse.

3.2. Results and discussion

The results of this measurement series are presented in Fig. 2. Subfigure 2(a) shows the observed interference signal (black solid lines with dots) for a delay interval from -65 fs to $+65$ fs scanned with a step size of 100 as along with the corresponding calculated interference signal (red solid lines). The outcome of the measurement is a high-quality 1st order interferometric autocorrelation trace of the oscillator pulses with a nearly perfect center to background ratio of 2:1. As a result of the inherent spatial overlap of the two pulses, an excellent contrast is obtained. The marginal offset visible in the measured interference signal is an effect occurring for all pulse shapers based on pixelated LC-SLMs, i.e. the residual transmission results from the gaps dividing the pixels. It is 3 % in our measurements being in agreement with the value expected from the geometric ratio of the width of interpixel gaps ($3.05 \mu\text{m}$) and the width of the active area of a single pixel ($96.52 \mu\text{m}$). The side wings present in the signal are due to the facts that the broad spectrum of the oscillator pulses is not perfectly symmetric and, in addition, slightly narrowed by the apertures of the optics in the pulse shaper (cf. spectral transmission window given in Subsect. 2.1). The spectrum of the oscillator pulses after passing the pulse shaper obtained for a flat phase applied to both layers of the LC-SLM is displayed in the inset to Fig. 2(a). It was measured with a wavelength- and intensity-calibrated spectrometer. Both aspects, the asymmetry as well as the spectral narrowing are visible. The M-shape of the oscillator spectrum is optimized for a subsequent amplification process.

The calculated interferometric autocorrelation trace shown in Subfigure 2(a) was determined according to the Wiener-Khinchine theorem [34]. It is obtained by Fourier transform of the spectrum shown in the inset. This calculated trace provides an independent check of the accuracy, because the spectrum determines the oscillation period of the interferometric autocorrelation. A comparison of measured and calculated traces shows an excellent agreement between these interferograms and their periodicities confirming the correct calibration of the absolute value of the phase of our pulse shaper.

For the next step in this measurement series a smaller delay interval ranging from -3 fs to $+3$ fs was selected and the delay step size was reduced to 10 as. The measured interference signal consists of approximately two oscillation periods (see Fig. 2(b)). In the delay range from -2.5 fs to -1.5 fs (indicated by the yellow-shaded area), between a maximum and a minimum of the interference signal, a strictly monotonic decreasing signal with decreasing absolute value of the pulse-to-pulse delay is expected. In Fig. 2(c) the measurement result for a scan of this range with a further reduced delay step size of 2 as is shown. In addition, for better visibility, the inset displays a zoom into a small interval. It reveals, that for the chosen delay step size the interference signal has the strictly monotonic behavior. This measurement demonstrates, that the precision achievable in the adjustment of the temporal separation of the two pulses is well below 2 as. In order to explore the limit in temporal resolution, a delay interval with a length of 12 as centered at $\tau = -2.025$ fs was selected and scanned with a delay step size of $0.1 \text{ as} = 100 \text{ zs}$. Due to the small range of this interval, the relation between signal S and pulse-to-pulse delay τ is approximately linear. The result of this measurement is illustrated in Fig. 2(d). Minute deviations from perfect monotony appear revealing that this delay step size is beyond the highest possible temporal resolution.

In order to find an estimation for the limit, we fitted a linear function S_{fit} (see Eq. (7) in the appendix) to the 100 zs step size measurement data. The fit curve allows us to calculate the standard deviation σ_τ of the pulse-to-pulse delay τ . The evaluation procedure is described in detail in the appendix. Applying this procedure to the measurement with 100 zs delay step size,

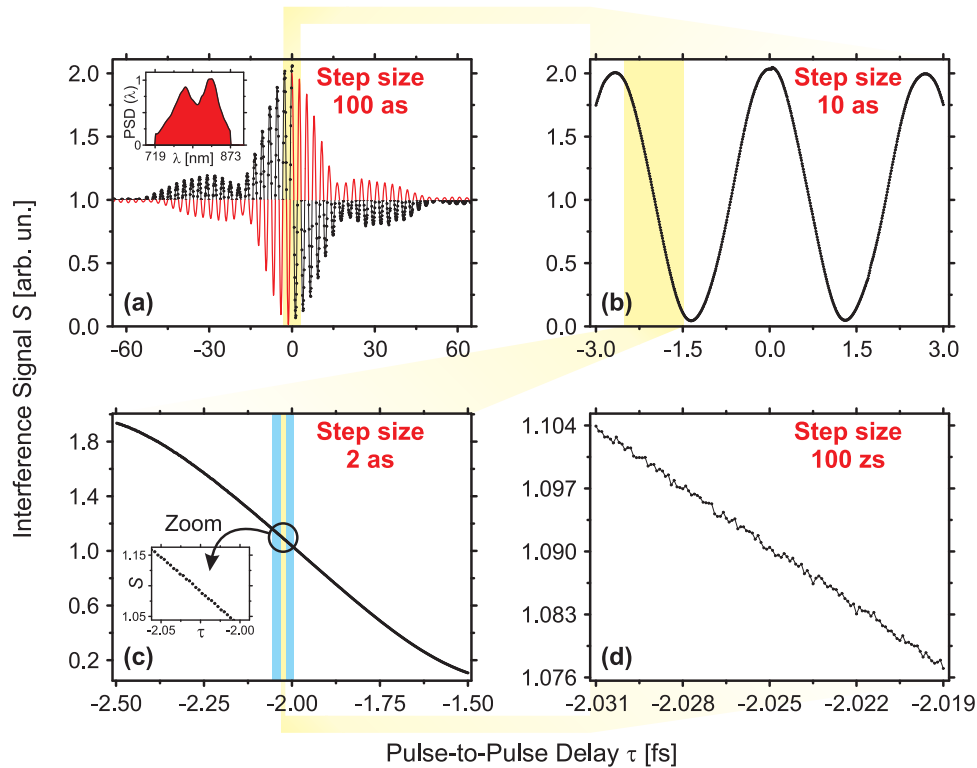


Fig. 2. (Color online) Interference signal S of two femtosecond laser pulses as a function of the pulse-to-pulse delay τ (1st order interferometric autocorrelation). The pulse pair is generated using the pulse shaper to mimic an ultrastable high-precision interferometer. The subfigures show measurement results for different delay intervals with successively decreasing ranges and delay step sizes: Scan of the delay in the range from (a) -65 fs to $+65$ fs with a step size of 100 as, (b) -3 fs to $+3$ fs with a step size of 10 as, (c) -2.5 fs to -1.5 fs with a step size of 2 as, and (d) -2.031 fs to -2.019 fs with a step size of 0.1 as = 100 zs. In (a) the measured signal (black solid lines with dots) is shown along with the calculated trace (red solid lines) resulting from the Fourier transform of the spectrum for comparison. The calculated interferogram serves as an independent check of the accuracy of the pulse shaper's phase calibration (for details see text). The yellow-shaded areas indicate the iteration steps in the delay ranges used from measurement to measurement. For a delay step size of 2 as a strictly monotonic decreasing interference signal is obvious (see inset in (c)), whereas for a step size of 0.1 as deviations from a monotonic behavior occur (d). The final limit in temporal resolution lies between 100 zs and 2 as.

we obtain a standard deviation of the pulse-to-pulse delay of $\sigma_{\tau} \approx 140$ zs. This leads to an estimation of the limit in minimum achievable delay step size of $2\sigma_{\tau} \approx 280$ zs.

In order to confirm this result in the experiment, we carried out an additional measurement using a delay interval ranging from -2.055 fs to -1.995 fs (blue-shaded area in Fig. 2(c)) and employing a delay step size of 300 zs. Figure 3 shows the result of this measurement. Essentially, a strictly monotonic behavior is observed, confirming the calculated limit of about 300 zs. We can express this temporal result in terms of an arm's length, which is varied in a Michelson- or Mach-Zehnder interferometer employing a delay stage. For a temporal precision

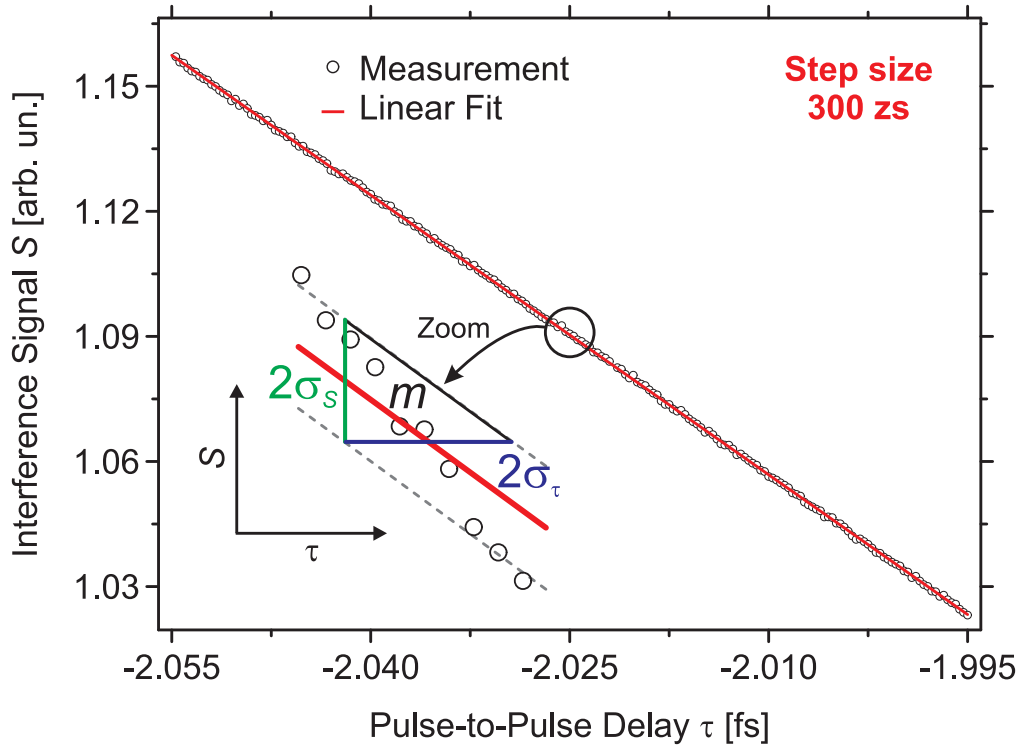


Fig. 3. (Color online) Interference signal S of two femtosecond laser pulses in dependence of the pulse-to-pulse delay τ . The delay is scanned within a 60 as interval from -2.055 fs to -1.995 fs (blue-shaded area in Fig. 2(c)) with a step size of 300 zs. The latter corresponds to the limit estimated from the data evaluation of the previous measurement with a delay step size of 100 zs (cf. Fig. 2(d)). Essentially, a strictly monotonic behavior of the interference signal is obtained. A linear fit to the measured data yields the slope m , which is associated with the standard deviations σ_S of the interference signal and σ_τ of the pulse-to-pulse delay as visualized in the inset. Using m and σ_S , we derive $\sigma_\tau \approx 150$ zs for the standard deviation of the pulse-to-pulse delay. Taking additionally the non-quantized Gaussian distribution of the residuals into account (cf. Fig. 4), we obtain $\delta_\tau \approx 11$ zs for the standard deviation of the mean.

of 300 zs a precision in mirror movement of 0.45 \AA is required, a length below the Bohr radius $a_0 = 0.529 \text{ \AA}$. The resolution of 300 zs is equivalent to nearly 10000 measurement points per oscillation period, which is about 2.67 fs for our experimental conditions. Applying the aforementioned fit procedure to the 300 zs delay step size measurement data yields $\sigma_\tau \approx 150$ zs for the standard deviation of the pulse-to-pulse delay. This confirms the value obtained from the measurement with 100 zs resolution.

In order to determine, whether the calculated standard deviation of the mean of $\delta_\tau \approx 11$ zs (cf. Eq. (10) in the appendix) is a meaningful quantity in our experiment, we consider the residuals for the optical interference measurement with 300 zs delay step size. They are the difference between the measured values and the linear fit to those data (cf. Eq. (7)). While in Fig. 4(a) the residuals are plotted, subfigure 4(b) is a histogram representation to reveal the nature of the residuals' distribution. We find a non-quantized Gaussian distribution confirming the standard deviation of the mean is a meaningful quantity here.

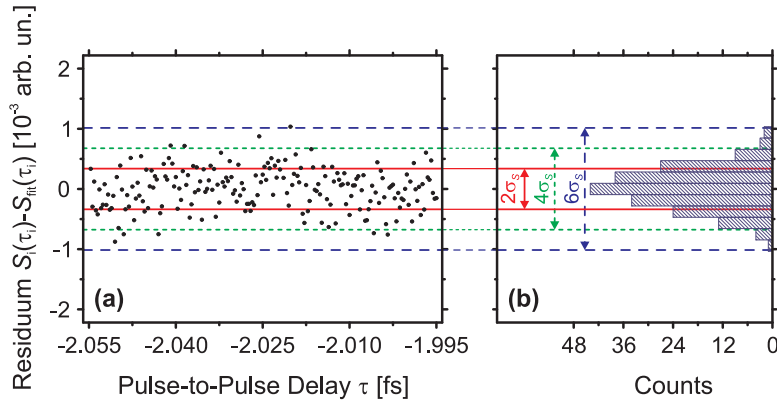


Fig. 4. (Color online) (a) Residuals given by the difference between the recorded values $S_i(\tau_i)$ for the interference signal measurement with a delay step size of 300 zs and the fit $S_{\text{fit}}(\tau_i)$ to those data. (b) The histogram representation of the same data exhibits a non-quantized Gaussian distribution of the residuals. The red solid lines, the green short-dashed lines and the blue long-dashed lines indicate intervals with ranges $2\sigma_S$, $4\sigma_S$ and $6\sigma_S$, respectively, including 68.3 %, 95.4 % and 99.7 % of all residuals.

4. Coherent quantum control experiment

4.1. Experimental

The objective of our quantum control experiment was to explore control of electron dynamics by a pair of femtosecond laser pulses, whose temporal separation is controllable down to the precision limit obtained in the all-optical experiment. In order to experimentally measure this limit we chose a well-defined physical system as a “benchmark”. To this end, we studied ultrafast coherent electronic excitation via resonant strong-field excitation and simultaneous multi-photon ionization of potassium atoms with intense shaped ultrashort laser pulses. It extends our previous work on the same quantum system [6, 35–38] with respect to the temporal accuracy by more than one order of magnitude.

In this experiment, we utilized an atomic transition, i.e. the corresponding induced oscillating dipole moment, to serve as an atomic ruler. In contrast to the all-optical experiment, we analyzed signals resulting from quantum interferences instead of recording optical interference signals from overlapping pulses. Here, the two pulses were temporally well-separated by around four times their pulse duration. Because there are no optical interferences, the energy of the two-pulse sequence does not depend on the phases applied to the pulse shaper, i.e. the power is constant. Therefore, the parameter relevant to exert control on the quantum system is exclusively the optical phase of the laser electric field. Manipulation of the relative phase between the two pulses allows us to tailor the shape of the electric field with respect to the dynamics of the atomic dipole.

In Fig. 5 the experimental setup is depicted along with the potassium excitation and ionization scheme. 30 fs FWHM laser pulses with a central wavelength of 790 nm provided by an 1 kHz multi-pass Ti:sapphire amplifier system (*Femtolasers Femtopower Pro*) pass a rotatable half-wave plate, the double layer LC-SLM based pulse shaper, and a polarizer. The laser pulses are attenuated to an energy of 0.5 μJ and focussed into a vacuum chamber by an $f = 300$ mm lens. The focusing conditions correspond to a pulse intensity of about 5×10^{11} W/cm². The laser beam perpendicularly intersects a potassium atomic beam generated in an adjacent oven chamber. Photoelectrons released during the light-atom interaction are collected and detected

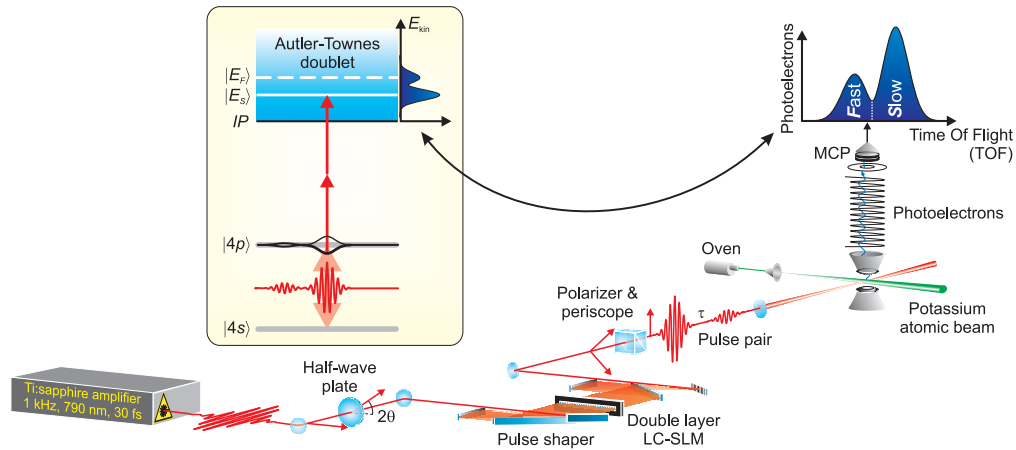


Fig. 5. (Color online) Schematic of the experimental setup for the coherent control experiment. The framed inset displays the excitation and ionization scheme of potassium atoms used as physical system. Ultrashort laser pulses provided by an amplifier system pass a half-wave plate, the double-layer LC-SLM based pulse shaper, and a polarizer. This setup enables the generation of pulse pairs with adjustable temporal delay τ and tunable energy ratio. These double pulses are focussed into a vacuum chamber to intersect a potassium atomic beam. The $4p \leftarrow 4s$ transition of potassium is strongly driven near resonance. Photoelectrons released during the light-atom interaction are measured by a magnetic bottle Time Of Flight spectrometer. The recorded photoelectron spectra exhibit the Autler-Townes doublet corresponding to an energy splitting of the resonant state into two dressed states due to strong-field excitation.

by an energy-calibrated magnetic bottle Time Of Flight (TOF) spectrometer. A more detailed description of the atomic beam preparation and the energy resolution of the spectrometer is found elsewhere [37]. Prior to the actual measurements on potassium, residual phase compensation of the initial pulses was performed in situ by adaptively optimizing the multi-photon ionization of ground state xenon atoms in the interaction region of the photoelectron spectrometer. In order to ensure transform-limited pulses, the resulting compensation phase was always applied to the LC-SLM in addition to the phase functions needed to generate the pulse pair.

By using suitable values for the pulse-to-pulse delay τ (cf. Eqs. (2)–(5)) and the rotation angle of the half-wave plate, a pulse pair consisting of a pre-pulse (approximately 2.3 % of the main pulse's intensity) and a much stronger main pulse is generated. The potassium transition $4p \leftarrow 4s$ is strongly driven by this pulse pair (cf. Fig. 5). The first pulse prepares the system in a state of maximum coherence. The strong-field excitation gives rise to an energy splitting of the resonant state into two dressed states, i.e. eigenstates of the total system comprising the two-level system and the excitation laser field. In addition, the second pulse ionizes the excited atom in a perturbative two-photon process mapping both the energy and the population of the dressed states into the photoelectron spectrum. This spectrum reveals the Autler-Townes (AT) doublet resulting from the energy splitting of the resonant state. The relative population of the dressed states and thus the branching ratio of fast (high kinetic energy E_F) and slow (low kinetic energy E_S) photoelectrons represented by the two peaks of the AT doublet depends on the relative optical phase between the two pulses, which is controlled by their temporal separation. The underlying strong-field control mechanism has been termed Selective Population Of Dressed States (SPODS), in this case realized via photon locking by temporal phase discontinuities. A detailed description of this scenario including a spatiotemporal picture is given in [36,37].

In this experiment the temporal separation between the two pulses was initially set to 120 fs. Then, in analogy to the all-optical experiment, the pulse-to-pulse delay and accordingly the relative phase between the two pulses was varied within different intervals with successively decreasing ranges and step sizes. Finally, the AT doublets in the photoelectron spectra recorded upon these scans are processed by calculating the AT contrast. It is given by

$$C_{\text{AT}} = \frac{F - S}{F + S}, \quad (6)$$

where F and S denote the integrated signals of fast and slow photoelectrons, respectively (cf. Fig. 5). This quantity is a measure for the asymmetry of the AT doublet and indicates the control exerted on the induced electron dynamics.

4.2. Results and discussion

The results of the quantum control experiment are illustrated in Fig. 6. We started with an initial pulse-to-pulse delay of $\tau = 120$ fs. In a first scan this temporal separation was varied by an amount ranging from 0 fs to 3.69 fs in steps of 41.5 as. This corresponds to a relative phase shift between the two pulses from 0 rad to 8.81 rad. The photoelectron spectra acquired during this scan are displayed in Fig. 6(a). The curve of the AT contrast C_{AT} calculated by processing the recorded spectra according to Eq. (6) is plotted in Fig. 6(c) together with the laser power. The photoelectron spectra as well as the contrast curve show evidence of the periodic switching between fast and slow photoelectrons as it was observed and discussed previously [36, 37]. Focusing on the yellow-shaded area in subfigure 6(c), the strictly monotonic behavior expected from the signal within this parameter range is observed in the experiment. This demonstrates the controllability of the underlying electron dynamics on a temporal level of the applied step size of 41.5 as.

In a second scan the interval indicated by the yellow-shaded area in Fig. 6(c) as well as the vertical dashed lines in Fig. 6(a) was investigated with higher resolution, i.e. the delay step size was reduced to 8.6 as. In this measurement the pulse-to-pulse separation was varied from 1.85 fs to 2.94 fs. This amounts to a relative phase shift from 4.4 rad to 7.0 rad. The measured photoelectron spectra along with the deduced contrast curve and the laser power are shown in Figs. 6(b) and (d), respectively. The results of this measurement with reduced step size show only slight deviations from strict monotony. This demonstrates, that the controllability is significantly increased down to the sub-10 as regime. Note, that the tendency of the contrast curve to decline with increasing pulse-to-pulse delay is a pure phase effect since the laser power was kept constant on a level of ± 1 % during these measurements. The power values plotted in addition reveal, that there is no overall correlation between AT contrast and residual laser fluctuations.

Because the setup for the coherent electronic excitation experiments is much more complex than the one for the all-optical investigations, it is more affected by noise and thus may suffer more severely from external perturbations. This results in the observed lower temporal precision. In particular, intensity fluctuations play a crucial role, because the branching ratio of the high and low energetic photoelectrons does not only depend on the relative phase between the used pulses, but it is also highly sensitive to variations of the intensity due to its non-trivial intensity dependence [6]. It has been shown, that the intensity of the first pulse or variations in the relative phase between the two pulses manipulate the branching ratio of the two AT components in a symmetrical fashion. Such intensity fluctuations may arise from residual laser power fluctuations within the aforementioned predefined interval of ± 1 % or from changes in the focusing conditions due to beam pointing.

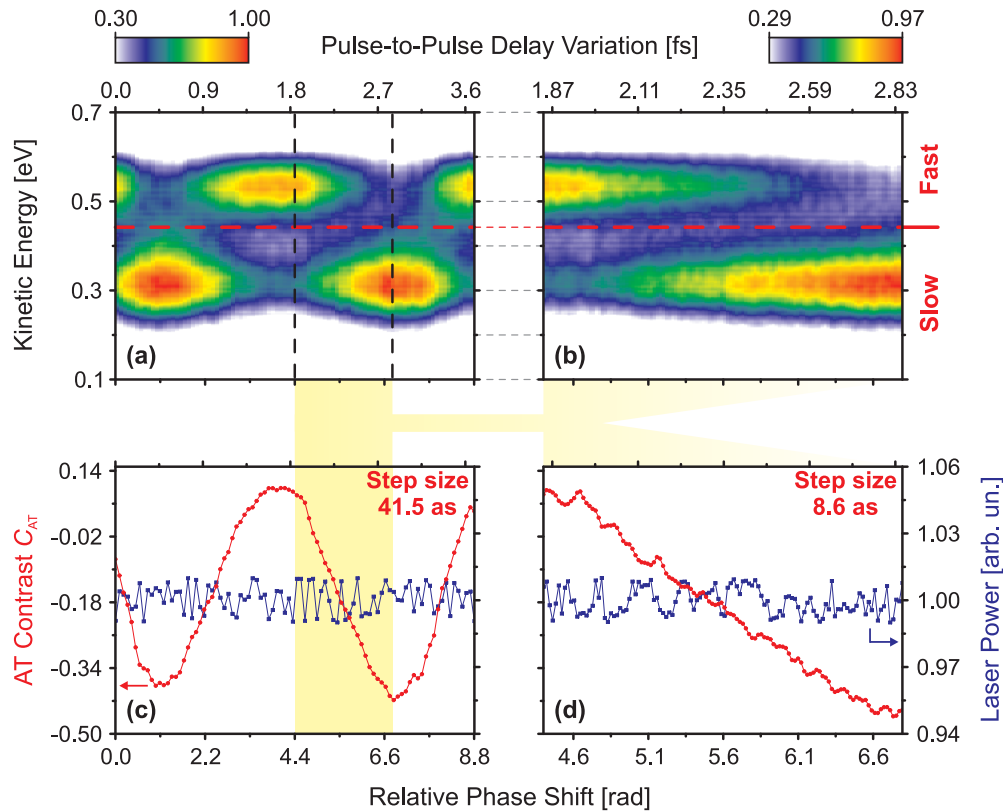


Fig. 6. (Color online) Results of the coherent quantum control experiment based on pulse pairs. The upper panel shows photoelectron spectra recorded as a function of the pulse-to-pulse delay variation and, hence, the relative phase shift between the two pulses. AT contrast curves deduced from the measured photoelectron spectra are displayed in the lower panel. The initial pulse-to-pulse delay of 120 fs was varied by an amount ranging from (a), (c) 0 fs to 3.69 fs (relative phase shift from 0 rad to 8.81 rad) with a step size of 41.5 as and (b), (d) 1.85 fs to 2.94 fs (4.4 rad to 7.0 rad) with a step size of 8.6 as. In addition to the periodic switching between fast and slow photoelectrons already visible in subfigure (a), the corresponding contrast curve (c) reveals the controllability of this process with a precision given by the step size of 41.5 as. This temporal precision can be increased significantly down to the sub-10 as regime as demonstrated by the contrast curve in (d). Only slight deviations from a monotonic behavior are present. The additionally plotted laser power, kept constant on a level of $\pm 1\%$, indicates, that there is no overall correlation between contrast signal and residual power fluctuations.

5. Application to attosecond pump-probe experiments

A promising application of the zeptosecond precision in the adjustment of the temporal separation between two femtosecond laser pulses presented in this paper, lies in the field of attosecond physics. Generally, efficient generation of isolated attosecond pulses is realized by high harmonic generation employing few-cycle femtosecond laser pulses. Pulse shaping of these very short femtosecond pulses has already been demonstrated [39] (and references therein). Applying our approach to mimic an interferometer by the use of a pulse shaper, a pair of temporally non-overlapping few-cycle femtosecond pulses can be produced, each of which is capable to

generate a corresponding attosecond pulse. By this means the temporal precision in pulse-to-pulse delay demonstrated here, is transferred to attosecond experiments and the associated timescale. This proposed scheme might pave the way to attosecond pump-probe experiments with extreme stability, highest precision and zeptosecond (sub-attosecond) temporal resolution. In addition, two attosecond pulses having polarization planes oriented orthogonally with respect to each other can also be generated using our scheme without the polarizer (cf. Fig. 1).

We note, that the polarization shaping capabilities of our pulse shaper also allow for the realization of the polarization gating approach to generate attosecond double pulses in the spirit of Oron et al. [40].

6. Summary and conclusions

We have presented an all-optical approach to implement an extremely stable high-precision common-path interferometer for ultrashort laser pulse applications based on spectral femtosecond pulse shaping techniques. Using a polarization pulse shaper to mimic the interferometer, we have investigated the temporal accuracy in the generation of ultrashort laser pulse pairs. In an all-optical experiment we have demonstrated a 2σ -precision of $300 \text{ zs} = 300 \times 10^{-21} \text{ s}$ in pulse-to-pulse delay with a standard deviation of the mean of 11 zs. In a coherent electronic excitation experiment we have applied precisely timed double pulses to strong-field quantum control with this technique. By steering population to different final quantum states with sub-10 as precision, we have shown efficient control of ultrafast electron dynamics in this temporal regime by employing our all-optical interferometer.

Ultrashort laser pulse pairs generated with the unprecedented precision in pulse-to-pulse delay as demonstrated in our measurements will be a useful tool in various research fields. The pulse shaper based interferometer is applicable to all experiments requiring precisely timed pairs of (shaped) ultrashort laser pulses ranging from femtosecond spectroscopy and high-precision coherent control to attosecond applications. For example, using the possibility of an extreme sub-cycle fine tuning of the pulse-to-pulse delay, the pulse shaper based interferometer will also be the ideal tool to probe highly nonlinear electronic coherences by strong-field sub-cycle interferometry [41]. In this scheme a pair of few-cycle femtosecond laser pulses is employed to resolve high order electron wave function beating.

Appendix

Our evaluation procedure to deduce the standard deviation σ_τ of the pulse-to-pulse delay for the measurement results shown in Figs. 2(d) and 3 in Subsect. 3.2 makes use of standard formulas of statistics. Here, they are recapitulated in detail for the sake of clarity.

In both of these measurements we consider delay intervals with ranges sufficiently small to approximate the interference signal S measured in dependence on the pulse-to-pulse delay τ by a linear fit function

$$S_{\text{fit}}(\tau) = m\tau + b. \quad (7)$$

This fit curve allows us to calculate the standard deviation σ_S of the measured interference signal S :

$$\sigma_S = \sqrt{\frac{1}{N-1} \sum_{i=1}^N [S_i(\tau_i) - S_{\text{fit}}(\tau_i)]^2} = \sqrt{\frac{1}{N-1} \sum_{i=1}^N [S_i(\tau_i) - (m\tau_i + b)]^2}, \quad (8)$$

where N is the number of measurement points. The slope m of the fit curve is associated with the standard deviation σ_S of the interference signal S from Eq. (8) as well as with the standard deviation σ_τ of the pulse-to-pulse delay τ by the equation

$$\sigma_S = |m| \sigma_\tau. \quad (9)$$

This relation is schematically depicted in the inset in Fig. 3. Inserting the values previously calculated for m and σ_S , we finally use Eq. (9) to extract a value for σ_τ .

Furthermore, for the measurement with a delay step size of 300 zs we additionally consider the standard deviation of the mean δ_τ . It is given by

$$\delta_\tau = \frac{\sigma_\tau}{\sqrt{N}}. \quad (10)$$

Acknowledgments

The financial support by the Deutsche Forschungsgemeinschaft DFG and the EU Marie Curie initial training network FASTQUAST is gratefully acknowledged.